

New solutions for periodic interfacial gravity waves

X. Guan¹, J.-M. Vanden-Broeck¹ and Z. Wang^{2,†}

¹Department of Mathematics, University College London, London WC1E 6BT, UK

²Institute of Mechanics, Chinese Academy of Sciences, Beijing 100190, PR China

(Received 18 June 2021; revised 24 August 2021; accepted 27 September 2021)

Two-dimensional periodic interfacial gravity waves travelling between two homogeneous fluids of finite depth are considered. A boundary-integral-equation method coupled with Fourier expansions of the unknown functions is used to obtain highly accurate solutions. Our numerical results show excellent agreement with those already obtained by Maklakov & Sharipov using a different scheme (*J. Fluid Mech.*, vol. 856, 2018, pp. 673–708). We explore the global bifurcation mechanism of periodic interfacial waves and find three types of limiting wave profiles. The new families of solutions appear either as isolated branches or as secondary branches bifurcating from the primary branch of solutions.

Key words: surface gravity waves

1. Introduction

It is well known that two-dimensional periodic surface gravity waves have a limiting configuration characterised by a sharp 120° angle at their crests. This is known as the Stokes highest wave. However, periodic interfacial gravity waves between two homogeneous fluids exhibit more complex limiting configurations. A local analysis indicates that the configuration of the Stokes highest wave in a two-fluid system inevitably results in an infinite velocity, and hence is not allowed (see e.g. Meiron & Saffman 1983). It was Holyer (1979) who first obtained solutions with a vertical tangent on the interface based on the Stokes expansion and Padé approximations. Subsequently, Saffman & Yuen (1982), Meiron & Saffman (1983), Pullin & Grimshaw (1983*a,b*) and Turner & Vanden-Broeck (1986) extended Holyer's results and found *Omega*-shaped profiles (multivalued solutions). Meiron & Saffman (1983) further asserted that these overhanging waves would develop into a self-intersecting profile as the limiting configuration but they did not compute them.

† Email address for correspondence: zwang@imech.ac.cn

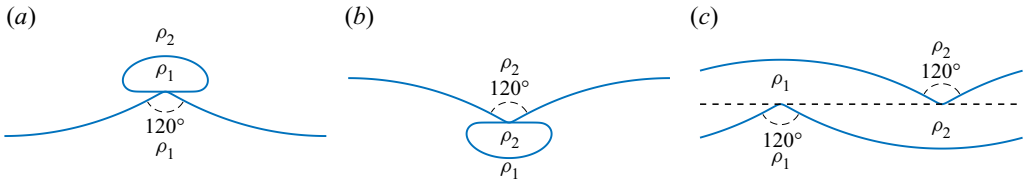


Figure 1. Three limiting profiles. We refer to them as (a) type I, (b) type II and (c) type III. Here, ρ_1 and ρ_2 are the heavier and lighter fluid densities, respectively.

Grimshaw & Pullin (1986) investigated the two-fluid system in the Boussinesq limit (i.e. the two fluids are of nearly equal density), when the lower layer is of infinite depth and the upper layer has a mean depth h and a constant vorticity ω . They found mushroom-shaped solutions and proposed a limiting configuration that features a closed bubble of heavier fluid on top of a 120° angle (see figure 1a). As $h \rightarrow \infty$ and $\omega \rightarrow 0$, they suggested a second limiting configuration, which consists of two inverted Stokes highest waves with a half-period phase shift and separated by a region of stagnant fluid (see figure 1c). This would come about as the periodic wave profile self intersected at four points in each period, effectively forming a four-layer system with two stagnant fluid regions cut off from the outer flow by the folded interface. When h is finite but relatively smaller than the wavelength, there is a third possibility. Although it was not indicated clearly by Grimshaw & Pullin (1986), some of their numerical results suggest the limiting configuration shown in figure 1(b), a closed bubble of lighter fluid underneath a downward 120° angle (i.e. the inversion of 1a). For convenience, the limiting configurations shown in figure 1(a–c) are hereafter termed type I, type II and type III limits, respectively. Although these results were obtained under special assumptions (infinite depth and non-zero constant vorticity), it turns out that they are valid in more general cases. For example, Maklakov & Sharipov (2018) developed a highly accurate numerical method based on the piecewise-analytical function theory, which provides solid numerical evidence for the existence of the type I limit when both layers are irrotational and infinitely deep.

In the present paper, periodic interfacial gravity waves in a two-layer system of finite depth are investigated numerically. The motion is assumed to be irrotational in each layer. We take a frame of reference moving with the wave, so that the flow is steady. Using the Cauchy integral formula and Fourier series, we obtain highly accurate numerical solutions which provide strong evidence for the existence of all three types of limiting configurations shown in figure 1. In the Boussinesq limit, we confirm the assertion of Grimshaw & Pullin (1986) on the type III solution by following the branch arising from a uniform flow (referred to as the primary branch), on which a secondary bifurcation point is found leading to type I and type II limits. The new branch isolates from the primary branch and gradually shrinks to zero when the density ratio is decreased from 1. Surprisingly, this novel bifurcation mechanism, i.e. the coexistence of three limiting types in one bifurcation diagram, can also be found in non-Boussinesq cases.

2. Mathematical formulation

Consider two-dimensional periodic interfacial waves propagating at a constant speed c between two incompressible, inviscid, irrotational and immiscible fluids that are bounded above and below by horizontal solid walls (see the schematic in figure 2). We denote by h_j and ρ_j ($j = 1, 2$) the depth and density in each fluid layer, where subscripts 1 and 2 refer to fluid properties associated with the lower and upper fluid layers, respectively. Assuming that the waves are symmetric, we choose a frame of reference moving with the wave and

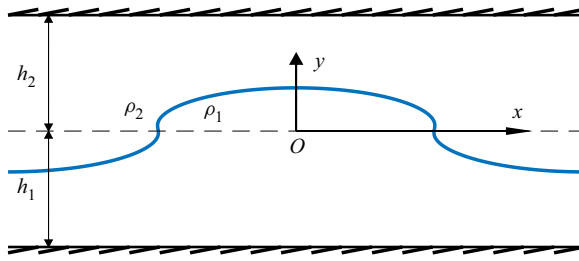


Figure 2. Schematic of the flow configuration. Here only one wavelength of the wave is sketched.

introduce a Cartesian coordinate system with the x -axis on the undisturbed interface and the y -axis on a line of symmetry (for example, a vertical line through a crest). The only restoring force under consideration is gravity which acts in the negative y -direction. It is convenient to choose ρ_1 , h_1 and c to be the units of density, length and velocity. Since the flow is irrotational in each fluid layer, we can introduce the velocity potentials ϕ_1 and ϕ_2 satisfying the Laplace equation

$$\phi_{1,xx} + \phi_{1,yy} = 0, \quad -1 < y < \eta, \tag{2.1}$$

$$\phi_{2,xx} + \phi_{2,yy} = 0, \quad \eta < y < h, \tag{2.2}$$

where η stands for the displacement of the interface and $h = h_2/h_1$ is the depth ratio. On the interface, the kinematic and dynamic boundary conditions read

$$\phi_{1,y} - \phi_{1,x}\eta_x = \phi_{2,y} - \phi_{2,x}\eta_x = 0, \tag{2.3}$$

$$R|\nabla\phi_2|^2 - |\nabla\phi_1|^2 + 2(R-1)\eta/F^2 = B, \tag{2.4}$$

where $R = \rho_2/\rho_1 < 1$ is the density ratio, $F^2 = c^2/(gh_1)$ the square of the Froude number, g the acceleration of gravity and B the Bernoulli constant.

3. Numerical methods

3.1. Boundary integral equations

We introduce a complex variable $\zeta = e^{-ikz}$, where k is the wavenumber and $z = x + iy$. This transformation maps the physical flow domain $[-\pi/k, \pi/k] \times [-1, h]$ onto an annular region in the complex ζ -plane (see, e.g. Papageorgiou & Vanden-Broeck 2004). Since the complex velocity $w = u - iv$ is an analytic function (u and v are the x and y components of the velocity), the Cauchy integral formula gives

$$w(\zeta) = \frac{1}{i\pi} \oint_C \frac{w(\zeta')}{\zeta' - \zeta} d\zeta', \tag{3.1}$$

where C represents the boundary of the upper or lower layer and ζ denotes a point on C . We can express w in terms of the velocity modulus q and the inclination θ as $w = qe^{-i\theta}$. Note that the relation between θ and the arclength parameter s takes the formula of $e^{i\theta} = dz/ds$. Using these notations, (3.1) can be rewritten as

$$w(\zeta) = -\frac{k}{\pi} \oint_C \frac{q}{1 - \zeta/\zeta'} ds. \tag{3.2}$$

Let $Y_+ = y(\sigma) + y(s)$, $Y_- = y(\sigma) - y(s)$, $X_+ = x(\sigma) + x(s)$ and $X_- = x(\sigma) - x(s)$. Applying the Schwarz reflection principle to (3.2) for both fluid layers and taking the

real part of equations, one then obtains

$$\begin{aligned} & \pi q_1(\sigma)x'(\sigma)/k \\ &= - \int_0^\alpha \left(\frac{q_1(s)(1 - e^{k(Y_+ + 2)} \cos(kX_-))}{1 + e^{2k(Y_+ + 2)} - 2e^{k(Y_+ + 2)} \cos(kX_-)} - \frac{q_1(s)(1 - e^{kY_-} \cos(kX_-))}{1 + e^{2kY_-} - 2e^{kY_-} \cos(kX_-)} \right) ds \\ & \quad - \int_0^\alpha \left(\frac{q_1(s)(1 - e^{k(Y_+ + 2)} \cos(kX_+))}{1 + e^{2k(Y_+ + 2)} - 2e^{k(Y_+ + 2)} \cos(kX_+)} - \frac{q_1(s)(1 - e^{kY_-} \cos(kX_+))}{1 + e^{2kY_-} - 2e^{kY_-} \cos(kX_+)} \right) ds, \end{aligned} \tag{3.3}$$

$$\begin{aligned} & \pi q_2(\sigma)x'(\sigma)/k \\ &= - \int_0^\alpha \left(\frac{q_2(s)(1 - e^{kY_-} \cos(kX_-))}{1 + e^{2kY_-} - 2e^{kY_-} \cos(kX_-)} - \frac{q_2(s)(1 - e^{k(Y_+ - 2h)} \cos(kX_-))}{1 + e^{2k(Y_+ - 2h)} - 2e^{k(Y_+ - 2h)} \cos(kX_-)} \right) ds \\ & \quad - \int_0^\alpha \left(\frac{q_2(s)(1 - e^{kY_-} \cos(kX_+))}{1 + e^{2kY_-} - 2e^{kY_-} \cos(kX_+)} - \frac{q_2(s)(1 - e^{k(Y_+ - 2h)} \cos(kX_+))}{1 + e^{2k(Y_+ - 2h)} - 2e^{k(Y_+ - 2h)} \cos(kX_+)} \right) ds, \end{aligned} \tag{3.4}$$

where α denotes the total arclength of the interfacial wave in half period and the assumed symmetry property of waves has been used.

3.2. The Fourier method

Due to the periodicity and symmetry of the computed waves, we can express the unknown functions as Fourier series. For convenience, we introduce a normalised arclength parameter $\tau = s/\alpha$ and write the Fourier expansions as

$$\left. \begin{aligned} q_1(\tau) &= \sum_{n=0}^\infty a_n \cos(n\pi\tau), & q_2(\tau) &= \sum_{n=0}^\infty b_n \cos(n\pi\tau), \\ x(\tau) &= c_0\tau + \sum_{n=1}^\infty \frac{c_n}{n\pi} \sin(n\pi\tau), & \eta(\tau) &= d_0 - \sum_{n=1}^\infty \frac{d_n}{n\pi} \cos(n\pi\tau). \end{aligned} \right\} \tag{3.5}$$

Truncating these series after N terms gives $4N$ unknowns, namely a_n, b_n, c_n and d_n ($n = 0, 1, \dots, N - 1$). Putting them together with F, B and α , there are eventually $4N + 3$ unknowns to be found. We evaluate (3.3) and (3.4) over the interval $[0, 1]$ at N equally spaced mesh points:

$$\tau_j = \frac{j - 1}{N - 1}, \quad j = 1, \dots, N. \tag{3.6}$$

To avoid the singularity in the Cauchy integral formula, we introduce another set of mesh grids:

$$\tau_j^m = \frac{\tau_j + \tau_{j+1}}{2}, \quad j = 1, \dots, N - 1, \tag{3.7}$$

and calculate the integrals by applying the midpoint rule. The Bernoulli equation and the arclength equation

$$Rq_2^2 - q_1^2 + 2(R - 1)\eta/F^2 = B, \tag{3.8}$$

$$x'^2 + \eta'^2 = \alpha^2 \tag{3.9}$$

are satisfied at the mesh points τ_j . Since the x -axis is fixed on the undisturbed interface level, we impose

$$\int_0^1 \eta(\tau)x'(\tau) \, d\tau = 0 \Rightarrow \sum_{n=1}^{N-1} \frac{c_n d_n}{2\pi n} + c_0 d_0 = 0. \tag{3.10}$$

To close the system, we also need to give a definition of the wave amplitude H :

$$H = \eta(0) - \eta(1), \tag{3.11}$$

and prescribe the wave speed c (which has been scaled to unity). There are different ways to define c . Following a widely used condition in surface gravity waves, we define c as the averaged velocity in the lower fluid

$$\frac{k}{\pi} \int_0^{\pi/k} u_1(x, y = \text{const.}) \, dx = -1, \tag{3.12}$$

where $y = \text{const.}$ is an arbitrary horizontal line within the lower layer. The negative sign reflects the fact that the background current is from right to left in the moving frame of reference. Equation (3.12) can be rewritten in terms of q_1 by using the irrotationality condition

$$\frac{\alpha k}{\pi} \int_0^1 q_1(\tau) \, d\tau = -1 \Rightarrow a_0 \alpha = -\frac{\pi}{k}. \tag{3.13}$$

In addition, a similar condition for q_2 is necessary for solving the problem:

$$b_0 \alpha = -\frac{\pi}{k}. \tag{3.14}$$

Although it is beyond the scope of this paper, it should be pointed out that the right-hand side of (3.14) can be an arbitrary constant, which can be thought of as giving different background current in each layer. Note that there are some extra conditions due to the symmetry of waves:

$$x(0) = 0, \quad \eta'(0) = 0, \quad \eta'(1) = 0, \tag{3.15a-c}$$

which are automatically satisfied owing to their Fourier representations. It is not difficult to verify that $c_0 = \pi/k$ due to the spatial periodicity of waves. Finally, we have $4N + 4$ (3.3)–(3.11) and (3.13)–(3.14) with only $4N + 2$ unknowns. Therefore, we choose to drop the equations of (3.3) and (3.4) at $\tau = 1$, and perform the Newton iteration to solve the system for given values of R , k , h and H . The iteration process is repeated until the maximum residual error is less than 10^{-10} . At first glance it seems dangerous to abandon two integral equations. However, our numerical results show that the maximum residual error of these two equations (denoted as δ hereafter) is of the order of 10^{-11} in most cases. Based on our numerical experience, $N = 600$ usually gives accurate enough results and thus is used in most computations. For almost-limiting solutions, however, typically 1200 Fourier modes are necessary to maintain appropriate accuracy and to ensure $\delta < 10^{-4}$.

4. Numerical results

4.1. Validation

In table 1, we present results for $R = 0.1$ and compare them with the works of Saffman & Yuen (1982) and Maklakov & Sharipov (2018). Since their results were obtained in

kH	C_s (S&Y)	C_s (M&S)	C_s ($N = 200$)	C_s ($N = 300$)
0.1	1.0010433	1.001043327	1.001043327	1.001043327
0.3	1.0093851	1.009385147	1.009385147	1.009385147
0.5	1.0260381	1.026038075	1.026038075	1.026038075
0.7	1.0509243	1.050924313	1.050924313	1.050924313
0.9	1.0839603	1.083960270	1.083960271	1.083960271
1.10	1.125454	1.125454593	1.125454593	1.125454593
1.20	1.149904	1.149903889	1.149903889	1.149903889
1.30	1.177	1.177754503	1.177754503	1.177754503
1.32	—	1.183901408	1.183901408	1.183901408
1.34	—	1.190327567	1.190327567	1.190327567
1.36	—	1.197125838	1.197125838	1.197125838
1.38	—	1.204514662	1.204514662	1.204514662
1.39	—	1.208645838	1.208645838	1.208645838
1.39	—	1.213326106	1.213326105	1.213326106
1.38	—	1.210675485	1.210675484	1.210675485
1.36	—	1.204401123	1.204401182	1.204401123
1.34	—	1.197369928	1.197369998	1.197369929
1.32	—	1.189740717	1.189740717	1.189740717
1.30	—	1.181506483	1.181506847	1.181506483
1.28	—	1.172510673	1.172523419	1.172510684

Table 1. C_s vs kH for $R = 0.1$, $h = 1$ and $k = 100$. The second and third columns are the results of Saffman & Yuen (1982) and Maklakov & Sharipov (2018), respectively.

the case when both layers are infinitely deep, we let $h = 1$ and $k \gg 1$ to achieve a good approximation of their results, and after many tests it was found that $k = 100$ is large enough to provide an excellent agreement. Note that these authors used a different length scale, $\sqrt{g/k}$, so their dimensionless wave amplitude reads kH . The dimensionless wave speed defined by Saffman & Yuen (C_s) and Maklakov & Sharipov (C_m) can be expressed as

$$C_s = F\sqrt{k}\sqrt{\frac{1+R}{1-R}}, \quad C_m = F\sqrt{k}. \tag{4.1a,b}$$

Increasing N up to 300, we have nine correct decimals in comparison with Maklakov & Sharipov (2018) in most cases except for a few solutions very close to the limiting configuration. Though not explicitly shown in table 1, for most solutions $\delta = O(10^{-11})$, which demonstrates the validity of our numerical method. Even when δ increases to $O(10^{-6})$, seven correct decimals can be guaranteed with $N = 300$.

4.2. Bifurcations and profiles

For any $R \in (0, 1)$, there is a branch of solutions bifurcating from infinitesimal periodic waves, which always leads to overhanging solutions. When $h \geq 1$, the limiting profiles of these branches are of type I and their geometry relies on the values of k and R . From a physical point of view, overhanging waves and associated limiting profiles would presumably suffer different instabilities (Kelvin–Helmholtz, Rayleigh–Taylor, etc.) and thus are difficult to be observed in experiments. However, our main concern here is the existence of limiting shapes which is separate from the question of instability. In figure 3, we show typical speed–amplitude bifurcation curves and related almost-limiting profiles for $h = 1$. The bubble features a half-lens shape and becomes horizontally long and

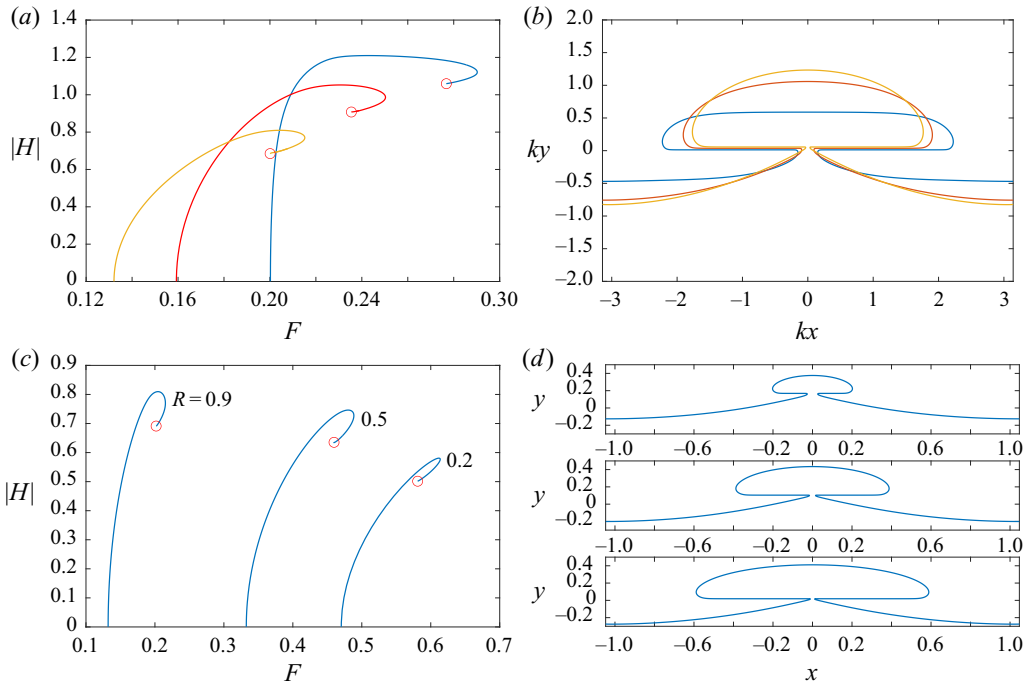


Figure 3. Typical speed–amplitude bifurcation curves and related almost limiting profiles. (a,b) $R = 0.9$, $h = 1$ and $k = 1$ (blue), $k = 2$ (red), $k = 3$ (yellow). (c,d) $k = 3$, $h = 1$ and $R = 0.2, 0.5, 0.9$. The corresponding almost-limiting profiles are plotted from top to bottom.

vertically thin when the value of k is gradually decreased for a fixed R . Note that to compare the profiles with different wavelengths, we rescale the horizontal and vertical coordinates by multiplying k , as shown in figure 3(b). On the other hand, for a given wavenumber k , the bubble enlarges when the value of R is increased, which is clearly demonstrated by figure 3(d). For general sets of parameters, bifurcation curves, along which almost-limiting profiles that are either of type I or of type II can be found. They appear qualitatively similar to those shown in figures 3(a) and 3(c). Guan *et al.* (2021) proposed a local model for the limiting configuration of type I for a small density ratio and calculated numerically profiles of the closed bubble. The almost-limiting profiles computed with the primitive equations when both layers are deep ($h = 1, k = 100$) and solutions of the simplified model are shown in figure 4. For comparison purpose, we make sure they match at the wave crest and flat bottom. The density ratios are $R = 0.1, 0.2$ and 0.3 from top to bottom and, as expected, the smaller density ratio gives a better agreement.

When $R \rightarrow 1$, i.e. the Boussinesq limit, Grimshaw & Pullin (1986) predicted the existence of the type III solution. This is intuitively reasonable since gravity is negligible and the wave profile should be invariant after being turned upside down, if one omits the possible phase shift. Maklakov & Sharipov (2018) also supported this assertion but did not provide direct numerical evidence. In the top diagram of figure 5(a), we display an almost-limiting solution in the Boussinesq limit ($R = 0.999999$) where $h = 1$ and $k = 100$ are used to approximate the condition that both layers are of infinite depth. This solution features a wave steepness of 0.1518π and a wave speed of 1.141 after being converted to the scaling of Grimshaw & Pullin (1986), which agree well with the corresponding values of 0.1411π and 1.0923 for the Stokes highest wave. It is also clear that the almost-limiting

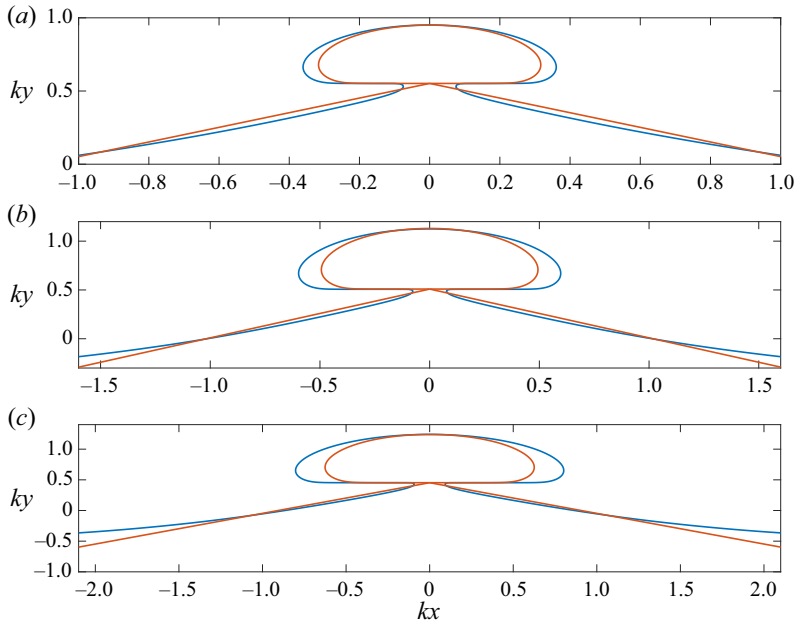


Figure 4. Comparisons between the almost-limiting solutions (blue) and solutions of the simplified model (red) from Guan *et al.* (2021). The parameters are chosen as $h = 1$, $k = 100$ and $R = 0.1, 0.2, 0.3$ from panels (a–c).

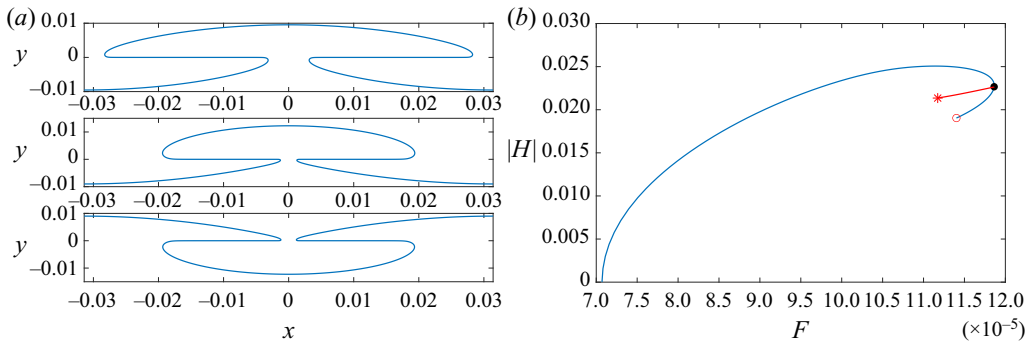


Figure 5. The bifurcation in the Boussinesq limit with $h = 1$, $k = 100$ and $R = 0.999999$. (a) Three almost-limiting profiles that correspond to type III, type I and type II limits from top to bottom. (b) A new speed–amplitude bifurcation branch (red) bifurcates from the primary one (blue) at a secondary bifurcation point (black dot). The circle relates to type III limit and the asterisk corresponds to type I and type II limits.

profile tends to become self-intersecting at both $x = 0$ and $x = \pm\pi/k$, hence yielding a limiting profile of type III. It is not surprising that the condition $k \gg 1$ is unnecessary to lead to such solutions, since the mirror symmetry with a possible phase shift relies only on the conditions $R \rightarrow 1$ and $h = 1$ (recalling that the lower layer has a unit depth).

However, it is found that the type III solution is not the only possible limiting profile in the Boussinesq limit. Other branches of solutions can arise through the secondary bifurcation mechanism as shown in figure 5(b). The blue curve is the primary branch bifurcating from infinitesimal periodic waves and the red circle denotes the almost-limiting configuration of type III (see the top figure of 5a). We check the Jacobian matrix along

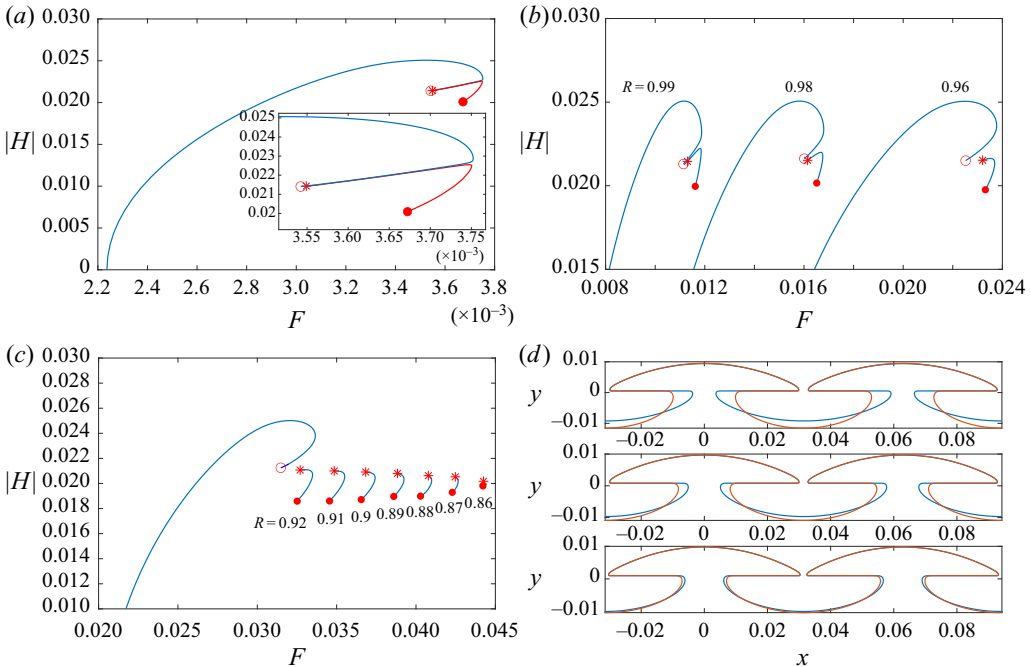


Figure 6. Speed–amplitude bifurcation curves and related almost-limiting profiles with $h = 1$ and $k = 100$. (a) $R = 0.999$. (b) $R = 0.99, 0.98, 0.96$. (c) A series of new bifurcation branches shrinking from left to right. The leftmost curve bifurcating from a uniform flow corresponds to $R = 0.92$. (d) Almost-limiting profiles with $R = 0.92, 0.88, 0.86$ from top to bottom. Blue and red profiles correspond to dots and asterisks in panel (c), respectively.

the primary branch and the solution is picked up as a candidate for the secondary bifurcation point if the matrix becomes nearly singular (interested readers are referred to Chen & Saffman (1980) for more details). It is shown in figure 5(b) that a secondary bifurcation point is found to exist (black dot), from which two coincident branches of new solutions (red curve) arise terminating at the limiting profiles of type I and type II. The almost-limiting profiles are labelled by the asterisk and plotted in the middle and bottom figures of 5(a). Therefore, limiting configurations of types I–III coexist in the Boussinesq limit for $h = 1$.

We take one of the secondary bifurcation branches as an example (the one which terminates at the type II limit, say) to explore its behaviour as R varies. If the value of R is slightly decreased, one can observe a separation of the secondary bifurcation curve from the primary branch as shown in figure 6(a). The isolated branch connects two limiting profiles labelled by a red dot and an asterisk, both of which are of type II. Three curves for $R = 0.99, 0.98, 0.96$ are shown in figure 6(b), from which one can see a growing distance between the isolated branch and the primary one as R is gradually decreased. Another striking feature is the shrinking tendency of these isolated curves as R decreases (see figure 6c). For $R < 0.86$, the new branch almost becomes a point, which indicates that these new solutions can exist only in a specific range of parameters. Therefore, it is also expected that the difference between the two limiting profiles at opposite ends of the isolated curve should gradually diminish as shown in figure 6(d), where blue and red curves correspond to dots and asterisks, respectively. It is worth mentioning that when the density ratio deviates from 1, the limiting configuration on the primary branch (labelled

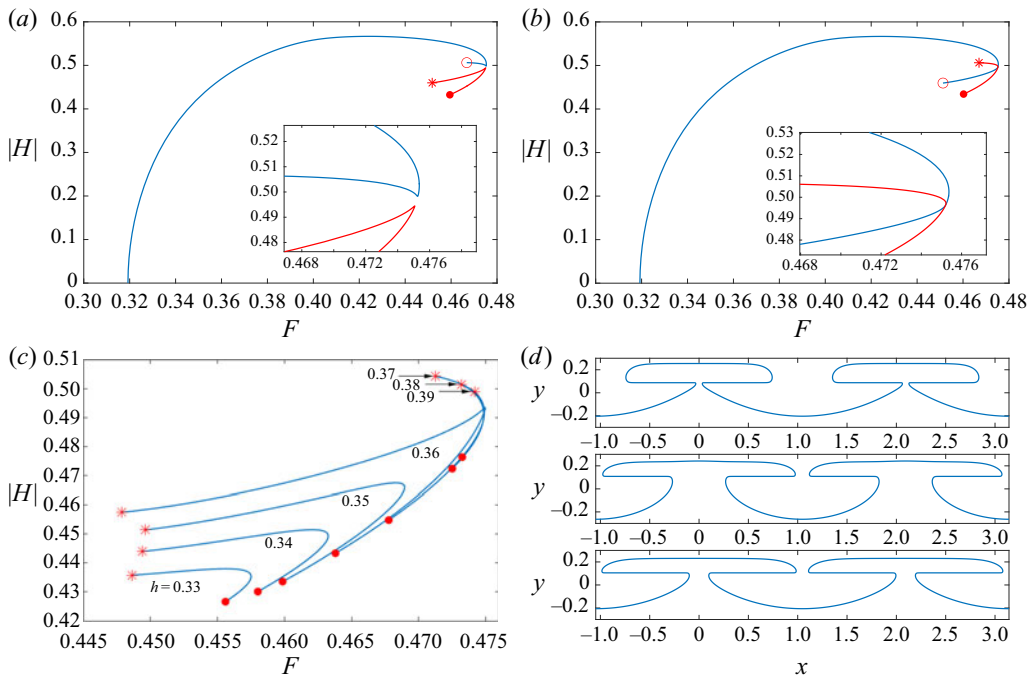


Figure 7. Speed–amplitude bifurcation curves and related almost-limiting profiles with $R = 0.5$ and $k = 3$. (a) $h = 0.3601$. (b) $h = 0.3602$. (c) A sequence of new bifurcation curves. (d) Three almost-limiting profiles corresponding to the asterisk, the circle and the dot in panel (a) from top to bottom.

by a red circle) becomes type I, and the readers should not associate these markers (circle, dot and asterisk) with any specific type of limit in general.

As discussed above, the existence of the secondary bifurcation and of the branch separation phenomenon is found near the Boussinesq limit. One can then ask whether or not this novel bifurcation mechanism exists in other situations. We give a positive answer to this question based on the numerical results shown in figure 7. For $k = 3$ and $R = 0.5$, it is found that there is a special depth ratio h_s for which three types of limiting solutions coexist and are linked via a secondary bifurcation point. Although the exact value of h_s is not easy to determine, the numerical evidence shown in figure 7(a,b) strongly suggests $0.3601 < h_s < 0.3602$ in this case. As h deviates from h_s , there are two types of branch separation depending on whether h is decreasing or increasing. There are three sub-branches arising from the secondary bifurcation point at $h = h_s$. When h is slightly below h_s , as shown in figure 7(a) for $h = 0.3601$, the top sub-branch stays on the primary branch (blue line) while the bottom two sub-branches form a new curve with a sharp corner (red line) which isolates from the primary one. Figure 7(b) shows the result for $h = 0.3602$ where the top and bottom sub-branches form a new curve (red line) breaking away from the primary branch (blue line). Note that although the two curves intersect at a common point in the parameter space as shown in figure 7(b), the two wave profiles at the intersection point are slightly different and this difference increases with h , indicating the branch separation phenomenon. A sequence of new bifurcation curves for different values of h are plotted in figure 7(c), which clearly shows a transition near 0.36. Almost-limiting waves akin to types I–III are labelled by the asterisk, circle and dot in figure 7(a) for $h = 0.3601$, and corresponding typical profiles are plotted in figure 7(d) from top to bottom.

5. Conclusion

In the present paper, we have investigated the bifurcation mechanism and limiting configurations of periodic interfacial gravity waves. Highly accurate numerical solutions have been obtained by applying a boundary-integral-equation method together with the Fourier representation of the unknown functions on the interface. Strong numerical evidence has been provided to support the existence of three kinds of limiting configurations as shown in [figure 1](#). New branches of solutions, which are either isolated or connected to primary branches via secondary bifurcation points, have been discovered in both the Boussinesq and non-Boussinesq cases. The new bifurcation mechanism can be understood as follows. At some critical points in the parameter space (k, h, R) , the secondary bifurcation occurs on the primary branch and three types of limiting configurations coexist in the same bifurcation diagram. As the parameter set deviates from the critical point, the new branch breaks away from the primary branch and gradually shrinks until it vanishes completely as the parameter set further varies.

Supplementary material. Supplementary material is available at <https://doi.org/10.1017/jfm.2021.854>.

Acknowledgements. X.G. would like to acknowledge the support from the Chinese Scholarship Council.

Funding. This work was supported by the National Natural Science Foundation of China under grant 11772341 and in part by EPSRC under grant EP/N018559/1.

Declaration of interests. The authors report no conflict of interest.

Author ORCIDs.

 Z. Wang <https://orcid.org/0000-0003-4393-2118>.

REFERENCES

- CHEN, B. & SAFFMAN, P.G. 1980 Numerical evidence for the existence of new types of gravity waves of permanent form on deep water. *Stud. Appl. Maths* **62**, 1–21.
- GRIMSHAW, R.H.J. & PULLIN, D.I. 1986 Extreme interfacial waves. *Phys. Fluids* **29** (9), 2802–2807.
- GUAN, X., VANDEN-BROECK, J.-M., WANG, Z. & DIAS, F. 2021 A local model for the limiting configuration of interfacial solitary waves. *J. Fluid Mech.* **921**, A9.
- HOLYER, J.Y. 1979 Large amplitude progressive interfacial waves. *J. Fluid Mech.* **93**, 433–448.
- MAKLAKOV, D.V. & SHARIPOV, R.R. 2018 Almost limiting configurations of steady interfacial overhanging gravity waves. *J. Fluid Mech.* **856**, 673–708.
- MEIRON, D.I. & SAFFMAN, P.G. 1983 Overhanging interfacial gravity waves of large amplitude. *J. Fluid Mech.* **129**, 213–218.
- PAPAGEORGIOU, D.T. & VANDEN-BROECK, J.-M. 2004 Antisymmetric capillary waves in electrified fluid sheets. *Eur. J. Appl. Maths* **15**, 609–623.
- PULLIN, D.I. & GRIMSHAW, R. 1983a Nonlinear interfacial progressive waves near a boundary in a Boussinesq fluid. *Phys. Fluids* **26** (4), 897–905.
- PULLIN, D.I. & GRIMSHAW, R. 1983b Interfacial progressive gravity waves in a two-layer shear flow. *Phys. Fluids* **26** (7), 1731–1739.
- SAFFMAN, P.G. & YUEN, H.C. 1982 Finite-amplitude interfacial waves in the presence of a current. *J. Fluid Mech.* **123**, 459–476.
- TURNER, R.E.L. & VANDEN-BROECK, J.-M. 1986 The limiting configuration of interfacial gravity waves. *Phys. Fluids* **29** (2), 372–375.